Anode Supported Planar 5 × 5 cm^2 $SrZr_{0.5}Ce_{0.4}Y_{0.1}O_{2.95}$ Based Solid Oxide Protonic Fuel Cells via Sequential Tape-Casting

Kwati Leonard [(ab)] *, Mariya E. Ivanova [(b)] *, André Weber[(c)] Wendelin Deibert[(b)], Wilhelm A. Meulenberg[(b)], Tatsumi Ishihara[(a)], Hiroshige Matsumoto [(a)]

[(a)] International Institute for Carbon-Neutral Energy Research (I2CNER), Kyushu University 744 Motooka, Nishi-ku, Fukuoka 819-0395, Japan

[(b)] Institute of Energy and Climate Research, Materials Synthesis and Processing (IEK-1), Forschungszentrum Jülich GmbH, Leo-Brandt-Str., D-52425 Jülich, Germany

[(c)] Institute for Applied Materials (IAM-ET), Karlsruhe Institute of Technology (KIT), Adenauerring 20b, Karlsruhe, Deutschland 76131, Germany

*E-mail of the Corresponding Author: kwati@i2cner.kyushu-u.ac.jp
*E-mail of the Corresponding Author 2: m.ivanova@fz-juelich.de

Abstract

Solid oxide protonic fuel cells are one of the most efficient means of directly converting stored chemical energy to usable electrical energy. Acceptor-doped Ba(Zr, Ce)O_3 perovskite-type oxides are the preferred electrolyte choice as they provide higher conductivity due to lower activation energy. While substantial progress has been made on small-sized protonic laboratory-scale cells, a considerable challenge has been upscaling robust planar-type devices. In this paper, a cost-effective inverse tape casting route and screen printing is employed to fabricate flat planar anode-supported protonic fuel cells consisting of NiO-$SrZr_{0.5}Ce_{0.4}Y_{0.1}O_{3-\delta}$ substrate, $SrZr_{0.5}Ce_{0.4}Y_{0.1}O_{3-\delta}$ electrolyte, and $BaCo_{0.4}Fe_{0.4}Zr_{0.1}Y_{0.1}O_{3-\delta}$ as the cathode. The processing parameters were analyzed and adjusted to obtain defect-free single cells of dimension up to 100 mm × 100 mm × 0.5 mm with diminished warping. In addition, the smooth tri-layered green tapes yielded suitably dense and gas-tight electrolyte layers after co-sintering at 1300 ºC/5h. Finally, the electrochemical performance of the 50 × 50 mm^2 $SrZr_{0.5}Ce_{0.4}Y_{0.1}O_{2.95}$ based cells was evaluated, and the impedance spectra were deconvoluted to identify all performance-related polarization processes via the distribution of relaxation time.

Keywords
Ceramic proton conductors; planar electrochemical cell; gas-tight solid oxide protonic electrolyte; protonic fuel cell; inverse/sequential tape casting

1. Introduction

Protonic ceramic fuel cells (PCFCs) are electrochemical devices that directly convert stored chemical energy to usable electrical energy with high efficiency[1–3]. Interest in these devices has continued to grow since the pioneering works of Iwahara in the 1980s on proton-conducting oxides[4–6]. Moreover, these devices operate at intermediate temperatures (400 ~600 °C), which simplifies sealing and slows down degradation[1,7,8]. In addition, water is produced at the cathode side during operation, avoiding fuel dilution, thus facilitating operation with high fuel utilization, contrary to regular solid oxide fuel cells (SOFCs)[8]. These benefits give PCFCs a comparative advantage in efficiency and cost over other fuel cell types. Currently, some of the most popular electrolytes for PCFCs are the acceptor-doped $Ba(Zr, Ce)O_3$ perovskite-type oxides[1,2,7,9–15], preferred for their higher conductivity due to lower migration barriers associated with Grotthuss-type proton diffusion[11]. As a result, PCFC performances with these electrolyte types have been impressively increased in recent years[2,16]. However, the most considerable drawback with this electrolyte class so far is its refractory nature, requiring relatively high sintering temperatures (≥ 1500 °C) to densify completely[7,12,15]. In addition, these high sintering temperatures commonly cause; i) Ba evaporation, which is detrimental to the electrolyte performance, ii) anode porosity loss, and iii) unwanted electrolyte/electrode interface reaction[12,14]. Although many recent studies have adopted sintering aids such as NiO[15,17,18], ZnO[19], CuO[20], etc., to facilitate densification by introducing a liquid phase for grain growth, this approach also negatively impacts the protonic concentration and favors the formation of undesired secondary phases. Therefore, it is imperative to minimize these sintering aids or adopt new strategies to lower the densification temperature.

A further challenge in PCFC development with this class of electrolytes has been scaling-up large area planar-type cells. This is a daunting task because the fabrication of such multi-layered type

cells requires careful control over chemical incompatibilities between the cell components, their sintering shrinkages, and thermal expansion coefficients to prevent warping and cracks [14,21]. Acceptor-doped Sr(Zr, Ce)O_3 -based perovskite-type oxides are alternative candidate electrolytes for these devices[22–27] due to their excellent mechanical and chemical stability. Even though their conductivity is about an order of magnitude lower than those reported for acceptor-doped Ba(Zr, Ce)O_3 perovskite-type oxides[9, 24], the ohmic losses from the electrolyte can be compensated by making the electrolyte layer relatively thinner.

In the present contribution, a cost-effective inverse tape casting route and screen printing are employed to fabricate large-area flat planar $SrZr_{0.5}Ce_{0.4}Y_{0.1}O_{3-\delta}$ (SZCY541) protonic cells on porous composite NiO-SZCY541 anodes substrate and $BaCo_{0.4}Fe_{0.4}Zr_{0.1}Y_{0.1}O_{3-\delta}$ (BCFZY) as the cathode. The processing parameters of the half-cell were analyzed and adjusted to obtain defect-free single cells of dimension up to 100 × 100 mm × 0.5 mm with diminished warping. The smooth tri-layered green tapes produced yielded suitably dense and gas-tight electrolyte layers after co-sintering at 1300 ºC/5h. Besides electrochemical characterization, the morphology and microstructure of the tri-layered half-cells were also analyzed. These results demonstrated that sequential tape casting is feasible for realizing low-cost fabrication of high-performing ceramic protonic cells.

2. Experimental

2.1 Sample preparation and characterization

SZCY541, BCFZY, and $BaZr_{0.44}Ce_{0.36}Y_{0.2}O_{3-\delta}$ (BZCY(54)$_{8/9}$2) powders were prepared by the chemical solution method as reported elsewhere[7], whereas Large quantities of SZCY541powders were also purchased from KUSAKA RARE METAL PRODUCTS Co. Ltd Japan. Powder X-ray diffraction patterns were recorded at room temperature to analyze the phase purity of the powders using a Rigaku X-ray diffractometer (XRD Ultima IV) with Cu-Kα radiations operating at 40 kV and 40 mA. Diffraction patterns were obtained in the 2θ range between 10º and 80º with a step size of 0.02º and

scan rate of 2° min^{-1}. Powder morphology, as well as external and fractured surfaces of the sintered half-cells, were observed by Field Emission-Scanning Electron Microscopy SEM (Hitachi High-Technologies SU8000 equipped with Energy-Dispersive X-ray Spectroscopy (Oxford INCA energy 300 EDS)

2.2 Cell fabrication and testing

The anode-supported Ni-SZCY541 substrates based half-cells were fabricated by sequential tape-casting using a KAROcast 300-7 micro-tape casting device (KMS Automation GmbH Germany). The substrate support slurry consisted of commercial NiO powder (Vogler, raw material) and SZCY541 (NiO, SZCY541, at a weight ratio of 60:40) dispersed in an ethanol and methyl ethyl ketone (MEK) mixture together with Nuosperse FX9086 (Elementis Specialties, Inc., London, UK) as the dispersing agent. In addition, polyvinyl butyral (Butvar PVB-98, Solutia Inc., St. Louis, MO, USA), Solusolv 2075 (Solutia Inc., St. Louis, MO, USA), and polyethyleneglycol PEG 400 (Merck Schuchardt, Hohenbrunn, Germany) also served as plasticizers and binder, respectively. The mixture was homogenized in a Thinky vacuum mixer and left to rest for 48 h to de-air and completely dissolve the binder before casting. The SZCY541 slurry was prepared using a previously reported two-step procedure[12,14] and cast onto a silicone-coated polymeric (Polyethylene terephthalate) foil. After proper drying at room temperature, a functional NiO-SZCY541 layer was cast directly on the SZCY541 layer, followed by the support NiO-SZCY541 slurry with a six hours interval for drying. This approach enables the formation of defect-free electrolyte layers given the foil's high surface quality. The as-fabricated green tapes were subsequently cut into appropriate dimensions and sintered at 1300°C for 5 h to obtain half-cells of sizes up to 100 × 100 mm × 0.5 mm (in the final-fired state). Co-firing the half-cells consisted of optimizing the heating ramps, de-binding, and subsequent sintering to achieve the desired microstructure. Thermo-gravimetric analysis (TGA) and differential thermal analysis (DTA) coupled with Mass Spectrometry (MS) were carried out using a Netzsch S.T.A. 409C system to understand the decomposition behavior of the organic additives in both the SZCY541

electrolyte and NiO-SZCY541 substrate single layers. The measurements were performed with a heating rate of 5 °C /min up to a maximum temperature of 1000 °C and in a constant flow of two gases: nitrogen and oxygen at ambient pressure. The warpage/bending behavior of the half-cell was investigated by comparing the shrinkage behavior of NiO-SZCY541, SZCY541 electrolyte, and the combined NiO-SZCY541 and SZCY541 electrolyte assembly using a TOMMI plus optical dilatometer (Fraunhofer I.S.C., Würzburg, Germany). The instrument consists of a furnace with quartz glass windows, a light source, and a charge-coupled device (CCD) camera. Samples for the shrinkage measurements were prepared by cutting off 15 × 20 mm strips from the respective green tapes and shaping them into cylinders. In addition, 28 mm diameter round-shaped green tape pieces were used for bending behavior investigations, using heating ramps of 1~4 °C/min and temperatures up to 1500 °C with dwell times of up to 3 h. Images of the sample silhouette were recorded every 60s with a camera during heat treatment. To further improve the mechanical properties of the half-cells, the combined NiO-SZCY541 and SZCY541 electrolyte assembly were laminated with a single substrate tape using a warm pressing. Lamination of tape layers was performed by applying pressure at 80 ºC until sufficient contact between the individual layers was formed.

Furthermore, as reported elsewhere[14], helium leak rate measurements were used to evaluate the electrolyte (50 × 50 mm^2) gas-tightness. The gas flow through the half-cell was determined with a mass spectrometer at a pressure difference of 1000 hPa. The values were normalized to a measured area of 16 cm^2 and a pressure difference of 100 hPa. Finally, a BCFZY cathode slurry prepared by mixing the powder in terpineol (5 wt% ethylcellulose) was screen-printed onto the SZCY541 electrolyte and sintered at 900 °C/2h to produce an active working electrode area of 1 cm^2. The resulting porous cathode exhibited a thickness of about 50 μm with homogenously distributed and well-connected fine particles.

2.3 Fuel cell electrochemical characterization.

Fuel cell electrochemical testing was carried out on the SZCY541 electrolyte-based single cells. The

cells were mounted into ceramic housings [28]. Gold mesh and Ni foam were used as the cathode and anode current collectors, respectively, whereas the cells were sealed with gold frames. The test housing and positions of voltage probes and current pick-up points have been previously described elsewhere[28,29]. Prior to the fuel cell operation, the gold frame sealant was heated at 900 ºC to obtain a gas-tight contact between the housing and the electrolyte. Then, the reduction of NiO to Ni in the anode cermet was performed at 600 °C. For the I/V-characteristics and impedance spectra, measurements, humidified H_2 (5% H_2O) and dry air with flow rates of 250 mL/m were used as the fuel and oxidant, respectively. Impedance measurements were carried out with a Solartron 1260 frequency response analyzer in a range of 100 m Hz to 1MHz. The amplitude of the current stimulus was chosen to achieve a voltage response not higher than 12mV. The measurements were performed at varied operation conditions. Impedance data analysis was performed utilizing the distribution of relaxation times (DRT), providing initial information about the electrochemical processes in the cells.

3. Results and discussions

3.1 Characterization of the ceramic powder

The quality of the ceramic powder for cell fabrication and scale-up depends strongly on the powder properties since they are known to strongly influence the microstructure of the cells in the final-fired state[12,14]. Table 1 presents the particle size and specific surface areas of the powders dispersed in the slurries used for tape-casting in this work. For example, the SZCY541 powder had a mean particle size d_{50} of 0.68 μm and a specific surface area (A_{spec}) of 3.1 m^2/g, which are satisfactory for making optimal slurries for tape casting[14,30,31].

Table 1. Mean particle size and specific surface areas of the powders for tape casting and processing temperature

Powder	Mean particle size (μm)			Specific surface area A_{spec} (m^2/g)	Calcination temperature (ºC)
	d_{10}	d_{50}	d_{90}		
SZCY541 Kasaka	0.50	0.69	0.95	3.1	1200
SZCY541 In-house	0.51	0.78	1.27	1.8	1200
BZCY(54)$_{8/9}$2 In-house	0.41	0.65	1.12	1.9	1300
NiO	0.50	0.70	1.10	2.4	N/A

Fig. 1(a). shows the X-ray diffraction patterns obtained at room temperature for SZCY541 and the composite NiO-SZCY541 powders, respectively. Indexing the patterns reveals that all the powders exhibit pure phases with minor impurities in agreement with previously reported data[9,23]. The diffraction patterns obtained on the SZCY541 electrolyte-based half-cell before and after sintering are presented in Fig. 1(b).

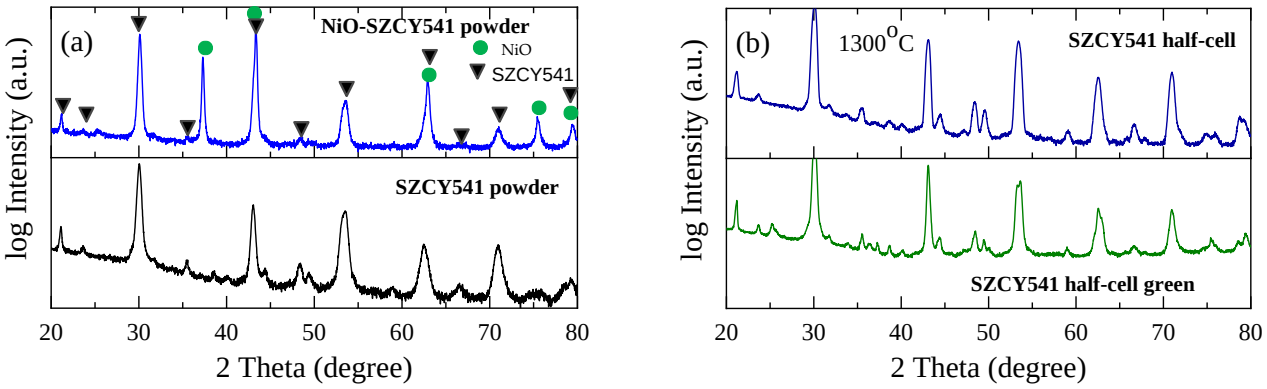

Fig. 1. (a) Room-temperature X-ray diffraction patterns of the as-prepared $SrZr_{0.5}Ce_{0.4}Y_{0.1}O_{3-\delta}$ power and NiO- $SrZr_{0.5}Ce_{0.4}Y_{0.1}O_{3-\delta}$ anode composite (b) Room-temperature X-ray diffraction patterns of $SrZr_{0.5}Ce_{0.4}Y_{0.1}O_{3-\delta}$ based green half-cell and the half-cell after sintering at 1300°C.

As observed, only diffraction peaks corresponding to the perovskite-structured SZCY541 electrolyte are detected as indexed by un-doped $SrCeO_3$ (CSD; 154927 ICSD) with no undesirable secondary phases. Furthermore, it is worth mentioning that no SrO island nor $SrCeO_3$-based phases can be seen by inspecting the SZCY541 top layer, even though Sr evaporation is remarkable at high temperatures[32].

3.2 Tape casting and characterization

The anode-supported NiO-SZCY541 and SZCY541electrolyte layers of the half-cell assemblies are fabricated using inverse/sequential tape casting[12,14,30]. Inverse tape casting presents an attractive, scalable, industrially established technology for manufacturing low-cost, large-scale ceramic

components with precisely controlled surface flatness. The approach requires optimally formulated ceramic slurries[14]. Half-cells were fabricated sequentially after proper layer slurries optimization. A detailed description are shown elsewhere[12,14,30]. First, a dense thin electrolyte SZCY541 layer with a solid loading of 25 vol. % was cast on a polymer foil, using an 80 μm doctor blade gap, and dried for about 6 h at room temperature. After which, the functional and substrate layers were cast successively on the electrolyte. With a drying interval of a few hours in between. We noted that pinholes and other defects are prone to appear on the electrolyte layer if the underlying sheet is not adequately dried and a subsequent layer is cast on top.

After casting, the green tapes were cut into 65 × 65 mm^2 and 130 × 130 mm^2 using a scalpel blade for subsequent characterization. Flat, 50 × 50 $mm^{2,}$ and 100 × 100 mm^2 planar half-cells, in the end, fired state were routinely obtained via this procedure. Table 2 summarizes the adjusted processing parameters during the fabrication process.

Table 2. Adjusted processing parameter during fabrication of half-cell

Layer	Blade gap [μm]	Casting speed [mm/s]	Drying time [h]	Green thickness [μm]	End-fired thickness [μm]
SZCY541 XTG	100	5	6	25	20
SZCY541 EL	80	5	6	19	~16
SZCY541 FL	45	10	5	12	~10
SZCY541 Asub	1200	2.5	10	~505	~400
XTG=specimen for TG analysis, EL=electrolyte, FL=functional layer, Asub= Anode substrate layer					

Given that the as-fabricated half-cells contain many organic additives, co-sintering of such layers generally requires an appropriate de-binding and sintering temperature program to avoid creating and propagating defects. Therefore, correctly understanding the organic additive's thermal behavior is essential to minimize undesirable defects such as cracks, or warpage, occurring during sintering. Fig. 2 presents TG/DTA curves for the SZCY541 electrolyte single layer. The curve shows two distinct mass changes corresponding to a total mass loss of 13.4 wt %. The initial significant mass change of 12.48 wt % recorded at ~172 to 302.8 °C is associated with an intensive release of the organic additives.

These temperature ranges also correspond with reported regimes for PEG-400, and PVB-98 burnout in green tapes, respectively[14,31]. Therefore, a low heating rate (0.5K min-1) within this temperature region was necessary to ensure a sufficiently slow release of all the tapes' organic constituents to provide defect-free ceramic layers.

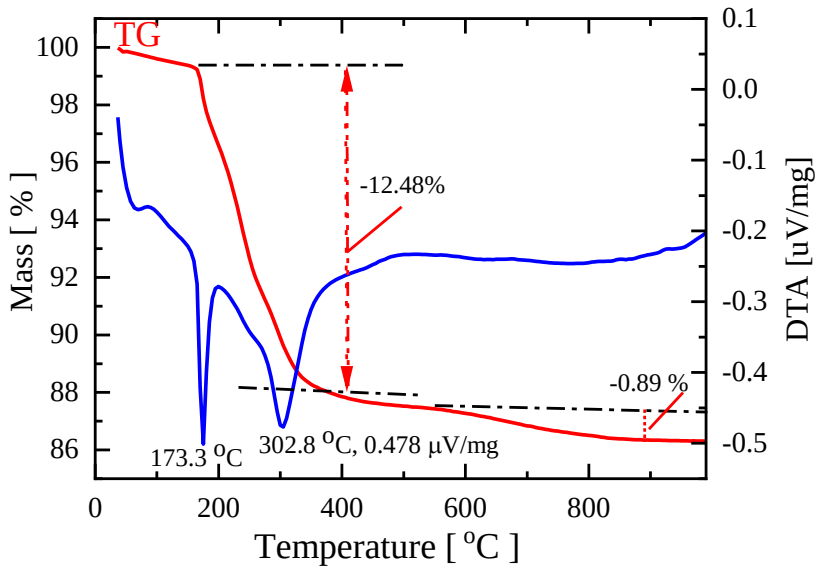

Fig. 2. Thermogravimetric measurement of $SrZr_{0.5}Ce_{0.4}Y_{0.1}O_{3-\delta}$ electrolyte green tapes in air, highlighting the decomposition behavior of organic additives with a heating rate of 0.5K min^{-1}

To further comprehend the evolved residual components during thermal decomposition, TG/DTA–MS analyses were also carried out on the NiO-SZCY541 single anode layer, as presented in Fig 4. A similar burnout characteristic with a significant mass decrease caused by the decomposition of the binder and the other additives was observed. The DTA curve shows three major endothermic peaks trenching to 189.8, 306.1, 330.7, and 408.5 °C. The first three peaks mirror the M.S. spectra at m/z = 17, 18, 26, 27, and 44 ion fragments. The m/z = 17, 18 are the characteristic values for the release of H_2O. Similarly, the m/z 44 (CO_2^+) curve is indicative of the release of CO_2. A sintering profile for the half-cells was thus formulated with a holding stage at 300 and 600 °C for 30 minutes to sufficiently burn out the additives.

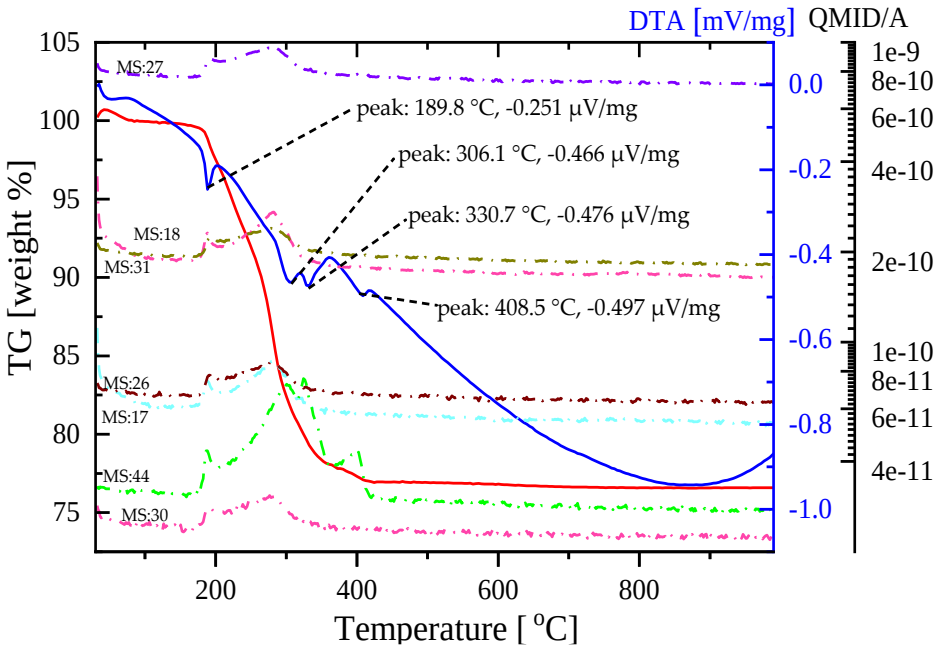

Fig. 3. Thermogravimetric mass spectrometric coupled analyses of NiO- $SrZr_{0.5}Ce_{0.4}Y_{0.1}O_{3-\delta}$ substrate with the total ion current plot of the evolved residues.

3.3 Sinterability of the half-cell and microstructure

Co-sintering of multi-layered half-cells is often challenging since the properties of the individual layers are inevitably affected by stresses due to shrinkage mismatch and the difference in sintering kinetics. The thermal behavior of SZCY541 and NiO-SZCY541 electrode assembly was further investigated using optical dilatometry. The sequence of shape evolution and bending behavior were observed using a charge-coupled device (CCD) camera during sintering of the half-cells. No apparent mismatch in sintering kinetic occurred on the SZCY541 and NiO-SZCY541 electrode assembly. Both layers showed a similar sintering behavior, which was beneficial to half-cell microstructure in the end-fired state. Suitably dense and gas-tight SZCY541 layers were routinely obtained after co-sintering round shape half-cells with Ø 28 mm diameter at 1300 °C for 5 hours. The observed sintering evolution behavior was also reproduced with the planar-type half-cell configuration (65 × 65 mm × 0.530 mm). The half-cell remained flat after sintering without cambers or warping, an observation that contrasts

the edge warpage demonstrated by the 50×50 mm^2 planar type BZCY(54)$_{8/9}$2 based half-cells previously reported[14]. The leak rate test of the half-cells with helium showed excellent gas tightness for both the flat 22 mm diameter and 50 × 50 mm^2 planar type SZCY541 electrolyte-based half-cells. An average leak rate of 6.83 × 10^{-6} hPa dm^3 (s cm^2)$^{-1}$ after sintering at 1350 °C/5h was obtained for the 50 × 50 mm^2 half-cells. This value is comparable and well within the threshold for high-quality reported SOFC gas-tight electrolytes[8,14]. Fig. 4 (a) presents the temperature program applied for 50 × 50 mm^2 SZCY541 planar half-cells sintering, whereas Fig. 4(b) depicts an image of a typical complete single cell.

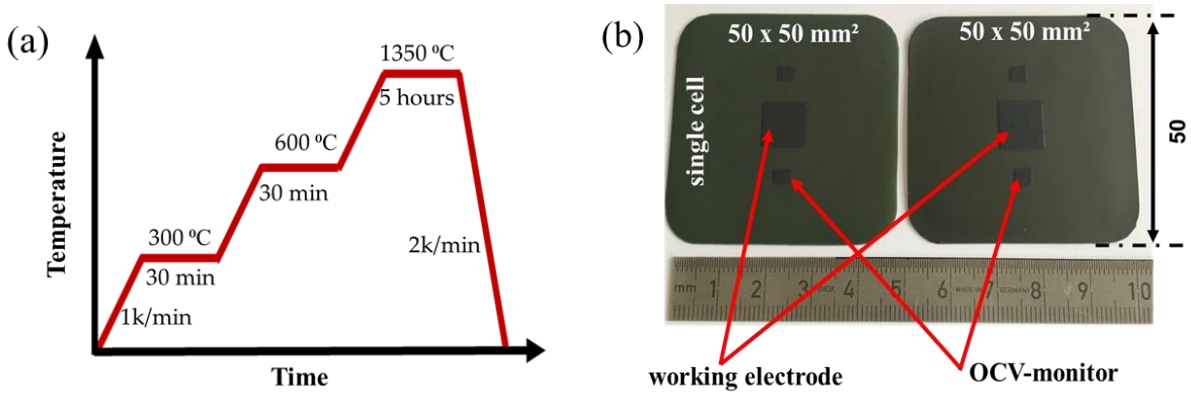

Fig. 4. (a) Temperature program applied for the 50 × 50 mm^2 SZCY541 planar half-cells sintering (b) Typical complete NiO- $SrZr_{0.5}Ce_{0.4}Y_{0.1}O_{3-\delta}$ |$SrZr_{0.5}Ce_{0.4}Y_{0.1}O_{3-\delta}$|$BaCo_{0.4}Fe_{0.4}Zr_{0.1}Y_{0.1}O_{3-\delta}$ cell used for fuel cell evaluation with the positions of voltage probes and current pick-up point.

As depicted in Table 2 above, the fabrication process produces a ~ 470 µm-thick electrolyte-electrode assembly with a 400µm thick anode support, ~16 µm-thick electrolyte, and ~50 µm-thick cathode. Fig. 5 shows the fractured cross-section and the morphology of the complete cell. As observed, the entire cell shows a well-organized, tri-layered structure without visible deformation, delamination, or cracks.

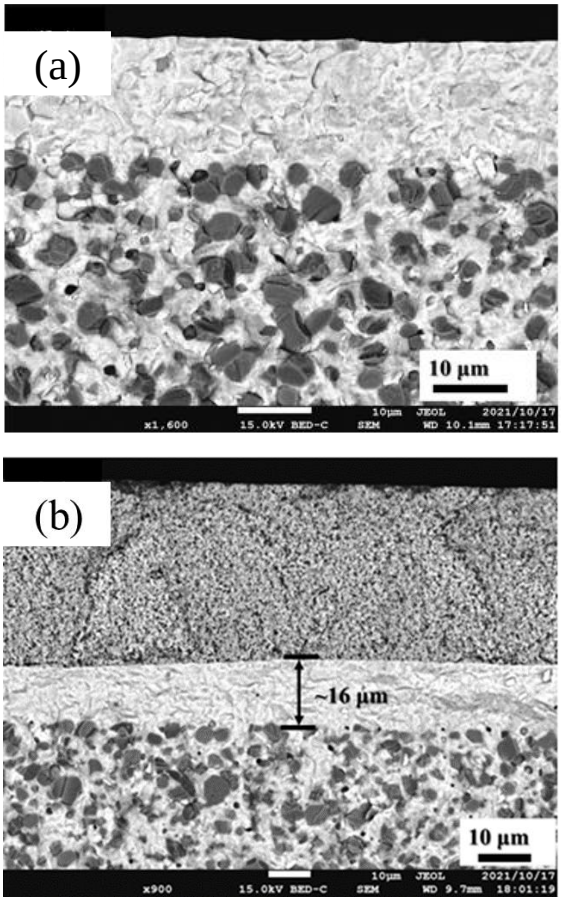

Fig. 5. (a) Typical microstructures of a half-cell in the final sintered state before reduction. (b) Scanning electron micrograph of the fracture cross-section of a typical complete cell showing the respective layers.

In addition, the NiO-SZCY541 layer adheres well to the SZCY541 layer forming an excellent percolating network, which should, in principle, lead to more triple-phase boundaries and thus enhance the anodic reaction. Finally, it is worth pointing out that there is no visible systematic contamination of the SZCY541 electrolyte layer by yttrium-rich secondary phase precipitates or strontium nickel oxides species.

3.4 Single-cell performance evaluation

The performance of the single-cells was evaluated at 600 ºC first to identify all performance-related

polarization processes. Fig. 6 (a) shows a typical I–V curve and the corresponding power density of the test cell (NiO-SZCY541 |SZCY541| BCFZY) under a supply of humidified H_2 (5%H_2O) to the anode and air to the cathode with flow rates of 250 mL/min and an operating temperature of 600 ºC.

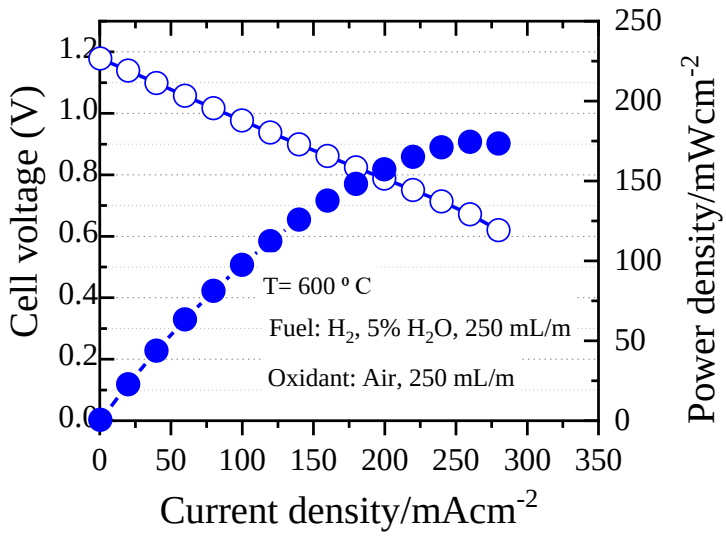

Fig. 6 (a) Typical I/V-characteristics of a single cell (NiO-SZCY541 |SZCY541| BCFZY) at 600 º C.

An open-circuit voltage of about 1.18 V is achieved on the main current pick-up point (working electrode as depicted in Fig.4(b). The two other voltage probes register 1.17 V, verifying that the electrolyte layer was dense enough to ensure gas tightness. The peak power density reached 172 mW cm^{-2} at 600 °C. Fig.7 shows a typical impedance spectrum measured at open circuit conditions that resolves ohmic R_Ω and polarization R_{pol} contributions to the cell's internal resistance. The electrolytes' ohmic resistance under OCV conditions was $0.89\,\Omega cm^2$ at 600 ºC, higher than that reported for the Y-doped Ba(Zr, Ce)O_3 perovskite-type oxides[7] because of the lower conductivity of the present SZCY541 electrolyte and its thickness.

Furthermore, as shown in Fig. 7 (b) below, the electrodes' polarization resistance dominates the total cell resistance. Hence, further reduction of the electrolyte thickness and improvement in the electrodes should boost the cell performance. The temperature dependencies of the former values correspond to

an Arrhenius behavior, exhibiting activation energies of 0.57 and 1.17 eV, respectively, for the temperature range between 450 and 650 ºC.

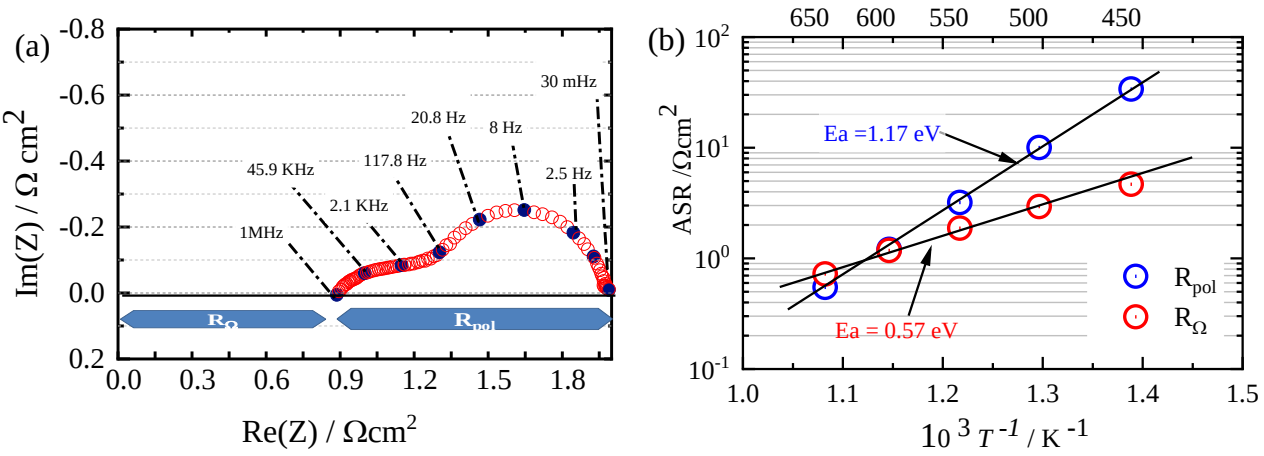

Fig. 7 Impedance spectrum resolving ohmic and polarization resistance of the cell (a) and temperature dependency of ohmic and polarization resistance (450 to 650 °C).

Impedance spectra were measured for different variations of fuel and oxidant composition. The subsequent analysis of the spectra data by the distribution of relaxation times (DRT) represents a powerful approach to unfold electrochemical processes in solid oxide cells. Figure 8 displays the DRTs for operating parameter variations described in ref.[29]. From the temperature variation (fig.8(a)), it is evident that all DRT-peaks are temperature dependent, showing a thermally activated behavior. This implies none of the peaks is solely related to a gas diffusion process. The gas diffusion in the substrate and the cathode are covered by other, thermally activated processes, and more elaborate procedures[33]are required to resolve and quantify them. Fig.8(b) reveals a strong impact of the oxidant composition on several peaks in the DRT. This suggests that the cathode is (i) responsible for a significant part of the polarization resistance, and (ii) its electrochemical behavior is describable by a transmission line model exhibiting several peaks in the DRT[28,29,34].

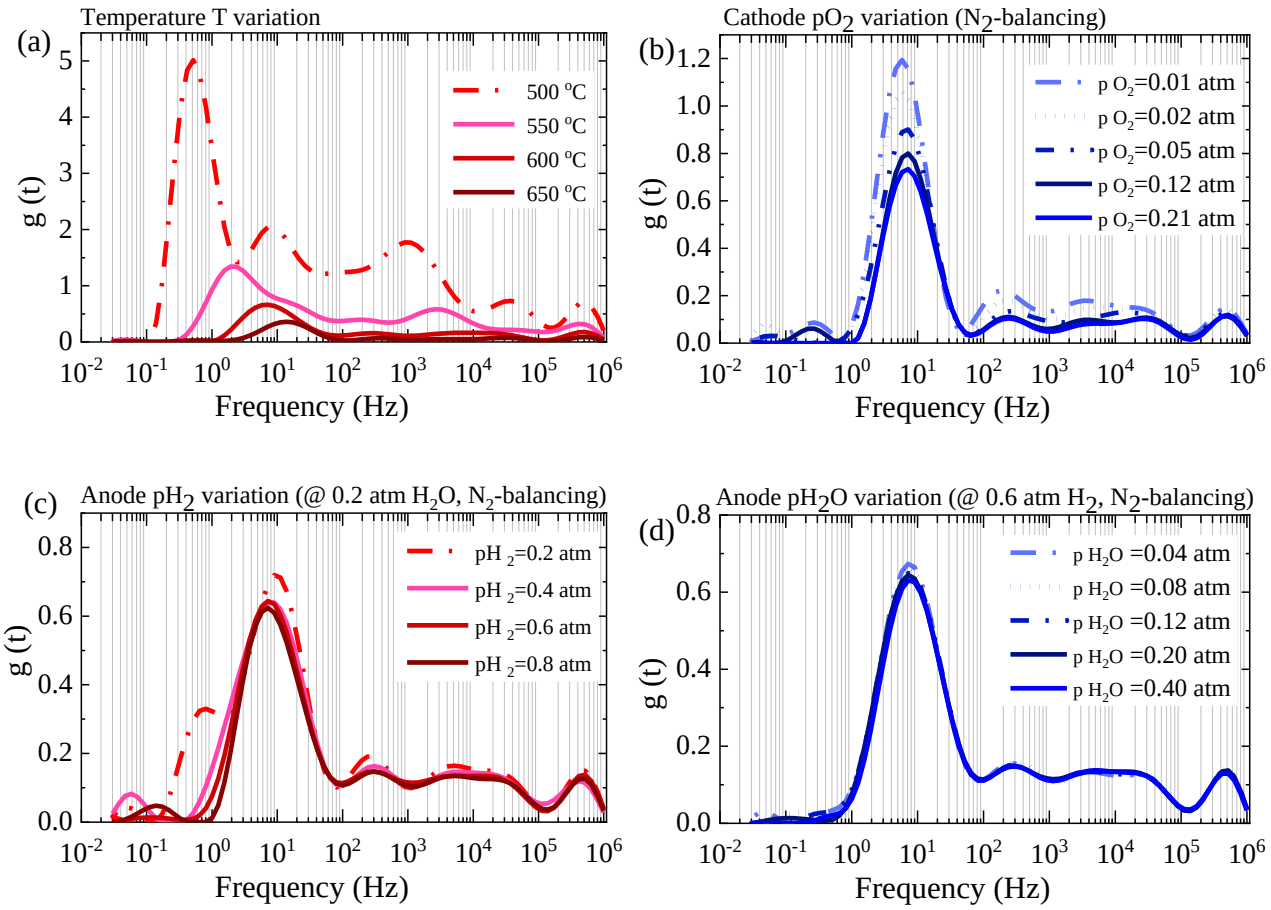

Fig. 8 DRTs of spectra measured during different operating parameter variations, (a) Temperature variation (b) the oxygen content in the oxidant, (c) hydrogen content in the fuel (d) steam content in the fuel are varied.

The hydrogen content in the fuel (Fig.8(c)) seems to impact the polarization resistance. Only minor changes are observable in the investigated range for 40 to 80% hydrogen, whereas an additional peak at 700 mHz appears at 20% hydrogen. The steam content in the fuel, which commonly shows a dominant impact on the anode polarization of state-of-the-art SOFCs with zirconia-based electrolytes, shows nearly no effect for the investigated PCC. This has to be attributed to the fact that the steam at the anode is not involved in the electrochemical reaction and thus behaves similar to an inert gas as nitrogen (here, it has to be considered that $pH_2O + pN_2 = const.$).

Further analysis of the electrochemical processes in the investigated PCC, including equivalent circuit

model development and model-based quantification of the losses, would require more additional experiments and will not be part of this contribution.

4. Conclusion

In summary, this paper presents the fabrication of a 50 × 50 mm^2 planar type $SrZr_{0.5}Ce_{0.4}Y_{0.1}O_{3-\delta}$ based ceramic fuel-cell using a scalable and industrially established inverse tape casting route. The processing parameters of the half-cell were analyzed and adjusted to obtain defect-free single cells of dimension up to 100 × 100 mm × 0.5 mm with diminished warping. The smooth bi-layered green tapes produced yielded suitably dense and gas-tight electrolyte layers after co-sintering at 1300 and 1350 ºC/5h for 22 mm diameter-based cells and the 50 × 50 mm^2 planar-type configuration, respectively. Furthermore, an open-circuit voltage of about 1.18 V is achieved, verifying that the electrolyte layer was dense enough to ensure gas tightness. Although not high, the peak power density reached 170 mW cm^{-2} at 600 °C and can be improved further by reducing the electrolyte thickness and improving the cathode microstructure. Finally, DRT calculations and analysis allowed us to identify the cathode responsible for a significant part of the polarization resistance in the cell. Future work will focus on cells' characterization with an active area of 16 cm^2 and developing strategies to mitigate electronic current leakages in PCFCs.

Acknowledgments

The authors gratefully acknowledge financial aid through JSPS KAKENHI Grant-in-Aid for Scientific Research (C), No. 19K05672, International collaboration work in the field of clean energy (NEDO No; 20001458-0) sponsored by the Ministry of Economy, Trade, and Industry (METI), Federal Ministry of Education, and Research BMBF, Germany under the funding reference 03SF0555A (Prometheus), the Helmholtz Association of German Research Centres, Germany, through the MTET Program and by the International Institute for Carbon-Neutral Energy Research (I2CNER) funded by the World Premier International Research Center Initiative (WPI), MEXT Japan.

Conflict of Interest

There are no conflicts to declare.

References

[1] H. Ding, W. Wu, C. Jiang, Y. Ding, W. Bian, B. Hu, P. Singh, C.J. Orme, L. Wang, Y. Zhang, D. Ding, Self-sustainable protonic ceramic electrochemical cells using a triple conducting electrode for hydrogen and power production, Nature Communications. 11 (2020). https://doi.org/10.1038/s41467-020-15677-z.

[2] S. Choi, T.C. Davenport, S.M. Haile, Protonic ceramic electrochemical cells for hydrogen production and electricity generation: Exceptional reversibility, stability, and demonstrated faradaic efficiency, Energy and Environmental Science. 12 (2019) 206–215. https://doi.org/10.1039/c8ee02865f.

[3] G. Yang, C. Su, H. Shi, Y. Zhu, Y. Song, W. Zhou, Z. Shao, Toward reducing the operation temperature of solid oxide fuel cells: Our past 15 years of efforts in cathode development, Energy and Fuels. 34 (2020) 15169–15194. https://doi.org/10.1021/acs.energyfuels.0c01887.

[4] H. Iwahara, T. Esaka, H. Uchida, N. Maeda, Proton conduction in sintered oxides and its application to steam electrolysis for hydrogen production, Solid State Ionics. 3–4 (1981) 359–363. https://doi.org/10.1016/0167-2738(81)90113-2.

[5] H. Matsumoto, I. Nomura, S. Okada, T. Ishihara, Intermediate-temperature solid oxide fuel cells using perovskite-type oxide based on barium cerate, Solid State Ionics. 179 (2008) 1486–1489. https://doi.org/10.1016/j.ssi.2008.02.048.

[6] H. Iwahara, H. Uchida, N. Maeda, High-temperature fuel and steam electrolysis cells using proton conductive solid electrolytes, Journal of Power Sources. 7 (1982) 293–301. https://doi.org/10.1016/0378-7753(82)80018-9.

[7] K. Leonard, Y. Okuyama, Y. Takamura, Y.S. Lee, K. Miyazaki, M.E. Ivanova, W.A. Meulenberg, H. Matsumoto, Efficient intermediate-temperature steam electrolysis with Y:$SrZrO_3$-$SrCeO_3$ and Y:$BaZrO_3$-$BaCeO_3$ proton conducting perovskites, Journal of Materials Chemistry A. 6 (2018) 19113–19124. https://doi.org/10.1039/c8ta04019b.

[8] D. Udomsilp, C. Lenser, O. Guillon, N.H. Menzler, Performance Benchmark of Planar Solid Oxide Cells Based on Material Development and Designs, Energy Technology. 9 (2021). https://doi.org/10.1002/ente.202001062.

[9] K. Leonard, Y.S. Lee, Y. Okuyama, K. Miyazaki, H. Matsumoto, Influence of dopant levels on the hydration properties of SZCY and BZCY proton conducting ceramics for hydrogen production, International Journal of Hydrogen Energy. 42 (2017) 3926–3937. https://doi.org/10.1016/j.ijhydene.2016.10.120.

[10] S. Barison, M. Battagliarin, T. Cavallin, L. Doubova, M. Fabrizio, C. Mortalò, S. Boldrini, L. Malavasi, R. Gerbasi, High conductivity and chemical stability of BaCe1-x-yZr xYyO3-δ proton conductors prepared by a sol-gel method, Journal of Materials Chemistry. 18 (2008) 5120–5128. https://doi.org/10.1039/b808344d.

[11] T. Norby, Solid-state protonic conductors: Principles, properties, progress and prospects, Solid State Ionics. 125 (1999) 1–11. https://doi.org/10.1016/S0167-2738(99)00152-6.

[12] W. Deibert, M.E. Ivanova, Y. Huang, R. Merkle, J. Maier, W.A. Meulenberg, Fabrication of multi-layered structures for proton conducting ceramic cells, Journal of Materials Chemistry A. 00 (2022) 1–12. https://doi.org/10.1039/d1ta05240c.

[13] T. Chen, Y. Jing, L.O. Anderson, K. Leonard, H. Matsumoto, N. Aluru, N.H. Perry, Toward Durable Protonic Ceramic Cells: Hydration-Induced Chemical Expansion Correlates with Symmetry in the Y-Doped BaZrO 3 –BaCeO 3 Solid Solution , The Journal of Physical Chemistry C. (2021). https://doi.org/10.1021/acs.jpcc.1c08334.

[14] K. Leonard, W. Deibert, M.E. Ivanova, W.A. Meulenberg, T. Ishihara, H. Matsumoto, Processing ceramic proton conductor membranes for use in steam electrolysis, Membranes. 10 (2020) 1–18. https://doi.org/10.3390/membranes10110339.

[15] Y. Huang, R. Merkle, J. Maier, Effects of NiO addition on sintering and proton uptake of Ba(Zr,Ce,Y)O3−δ, Journal of Materials Chemistry A. 9 (2021) 14775–14785. https://doi.org/10.1039/d1ta02555d.

[16] H. An, H.W. Lee, B.K. Kim, J.W. Son, K.J. Yoon, H. Kim, D. Shin, H. Il Ji, J.H. Lee, A 5 × 5 cm2 protonic ceramic fuel cell with a power density of 1.3 W cm–2 at 600 °C, Nature Energy. 3 (2018) 870–875. https://doi.org/10.1038/s41560-018-0230-0.

[17] E. Kim, Y. Yamazaki, S.M. Haile, H.I. Yoo, Effect of NiO sintering-aid on hydration kinetics and defect-chemical parameters of BaZr0.8Y0.2O3 - Δ, Solid State Ionics. 275 (2015) 23–28. https://doi.org/10.1016/j.ssi.2015.01.001.

[18] D. Han, K. Goto, M. Majima, T. Uda, Proton Conductive BaZr0.8-xCexY0.2O3-δ: Influence of NiO Sintering Additive on Crystal Structure, Hydration Behavior, and Conduction Properties, ChemSusChem. 14 (2021) 614–623. https://doi.org/10.1002/cssc.202002369.

[19] S. Tao, J.T.S. Irvine, A stable, easily sintered proton-conducting oxide electrolyte for moderate-temperature fuel cells and electrolyzers, Advanced Materials. 18 (2006) 1581–1584. https://doi.org/10.1002/adma.200502098.

[20] J.H. Lee, S.M. Choi, J.H. Lee, J. Hong, H. Kim, K.J. Yoon, B.K. Kim, Effect of sintering atmosphere on phase stability, and electrical conductivity of proton-conducting Ba(Zr0.84Y0.15Cu 0.01)O3-δ, International Journal of Hydrogen Energy. 39 (2014) 7100–7108. https://doi.org/10.1016/j.ijhydene.2014.02.072.

[21] L.Q. Le, C.H. Hernandez, M.H. Rodriguez, L. Zhu, C. Duan, H. Ding, R.P. O'Hayre, N.P. Sullivan, Proton-conducting ceramic fuel cells: Scale-up and stack integration, Journal of Power Sources. 482 (2021) 228868. https://doi.org/10.1016/j.jpowsour.2020.228868.

[22] H. Matsumoto, T. Sakai, Y. Okuyama, Proton-conducting oxide and applications to hydrogen energy devices, Pure and Applied Chemistry. 85 (2013) 427–435. https://doi.org/10.1351/PAC-CON-12-07-11.

[23] K. Leonard, J. Druce, V. Thoreton, J.A. Kilner, H. Matsumoto, Exploring mixed proton/electron conducting air electrode materials in protonic electrolysis cell, Solid State Ionics. 319 (2018) 218–222.

https://doi.org/10.1016/j.ssi.2018.02.016.

[24] Y. Okuyama, K. Isa, Y.S. Lee, T. Sakai, H. Matsumoto, Incorporation and conduction of proton in $SrCe_{0.9-x}ZrxY_{0.1}O_{3-\delta}$, Solid State Ionics. 275 (2015) 35–38. https://doi.org/10.1016/j.ssi.2015.01.010.

[25] S. Maeda, Y. Shiratori, D. Kurashina, T. Fujisaki, K. Leonard, H. Matsumoto, Electrochemical reforming of methane using SrZr0.5Ce0.4Y0.1O3-δ proton-conductor cell combined with paper-structured catalyst, International Journal of Hydrogen Energy. 45 (2020) 4026–4034. https://doi.org/10.1016/j.ijhydene.2019.11.211.

[26] Y. Takamura, K. Leonard, A. Luo, L.W. Martin, H. Matsumoto, Platinum nanoparticle-induced nano ionic effects on electrical conduction in strontium cerate and zirconate, Journal of Solid State Electrochemistry. 23 (2019). https://doi.org/10.1007/s10008-018-04188-z.

[27] T. Fujisaki, A.T. Staykov, Y. Jing, K. Leonard, N.R. Aluru, H. Matsumoto, Understanding the Effect of Ce and Zr on chemical expansion in yttrium doped strontium cerate and zirconate by high-temperature X-ray analysis and density functional theory, Solid State Ionics. 333 (2019). https://doi.org/10.1016/j.ssi.2019.01.009.

[28] D. Klotz, A. Weber, E. Ivers-tiffée, Electrochimica Acta Practical Guidelines for Reliable Electrochemical Characterization of Solid Oxide Fuel Cells, Electrochimica Acta. 227 (2017) 110–126. https://doi.org/10.1016/j.electacta.2016.12.148.

[29] A. Leonide, V. Sonn, A. Weber, E. Ivers-Tiffée, Evaluation and Modeling of the Cell Resistance in Anode-Supported Solid Oxide Fuel Cells, Journal of The Electrochemical Society. 155 (2008) B36. https://doi.org/10.1149/1.2801372.

[30] W. Deibert, M.E. Ivanova, W.A. Meulenberg, R. Vaßen, O. Guillon, Preparation and sintering behavior of La5.4WO12-δ asymmetric membranes with optimized microstructure for hydrogen separation, Journal of Membrane Science. 492 (2015) 439–451. https://doi.org/10.1016/j.memsci.2015.05.065.

[31] M.E. Ivanova, W. Deibert, D. Marcano, S. Escolástico, G. Mauer, W.A. Meulenberg, M. Bram, J.M. Serra, R. Vaßen, O. Guillon, Lanthanum tungstate membranes for H2 extraction and CO2 utilization: Fabrication strategies based on sequential tape casting and plasma-spray physical vapor deposition, Separation and Purification Technology. 219 (2019) 100–112. https://doi.org/10.1016/j.seppur.2019.03.015.

[32] B. Koo, K. Kim, J.K. Kim, H. Kwon, J.W. Han, W.C. Jung, Sr Segregation in Perovskite Oxides: Why It Happens and How It Exists, Joule. 2 (2018) 1476–1499. https://doi.org/10.1016/j.joule.2018.07.016.

[33] C. Grosselindemann, N. Russner, S. Dierickx, F. Wankmüller, A. Weber, Deconvolution of Gas Diffusion Polarization in Ni/Gadolinium-Doped Ceria Fuel Electrodes, Journal of The Electrochemical Society. 168 (2021) 124506. https://doi.org/10.1149/1945-7111/ac3d02.

[34] A. Weber, Fuel flexibility of solid oxide fuel cells, Fuel Cells. 21 (2021) 440–452. https://doi.org/10.1002/fuce.202100037.